JOURNAL OF MAGNETIC RESONANCE, Series A 101, 240–248 (1993)

Position–Displacement Correlations in Fluids from Magnetic Resonance Gradient-Echo Shapes

LUCIO FRYDMAN, JOHN S. HARWOOD,* DARREN N. GARNIER,† AND GERARD C. CHINGAS‡

Materials Sciences Division, Lawrence Berkeley Laboratory, Berkeley, California 94720

Received November 13, 1991; revised July 9, 1992

A nuclear magnetic resonance technique providing slice-selected spatial distribution of fluid displacements is introduced and exemplified. This echo-shape analysis method exploits the fact that, in a pulsed-gradient spin-echo sequence, the phase encoding of the echo evolves from a position dependence at the start of this pulse to a displacement dependence at the echo peak. The shape of the forming echo is therefore determined by the joint probability distribution correlating initial particle positions with displacements occurring between the first and the second gradient pulses. This distribution may be directly extracted by Fourier analysis of the echo shape as a function of gradient level. This procedure provides efficient access to Lagrangian flow statistics, as is illustrated by application to Taylor–Couette flow. Agreement between experimental results and simulations demonstrates the suitability of this method for examining spatially heterogeneous flow and molecular transport processes.

INTRODUCTION

Wide interest in flow stems from the central role of transport processes in medical and biological processes as well as in physical and chemical changes. Nuclear magnetic resonance of systems moving in an applied field gradient has proven to be especially useful (*1–4*) due to its noninvasive character and relative independence from the fluid optical properties. Although varied approaches using fixed (*5–8*) and oscillating (*9*) gradients have been discussed, the traditional approach is the pulsed-gradient spin-echo (PGSE) experiment of Stejskal and Tanner (*10, 11*).

This sequence, shown in Fig. 1, starts with a 90° radio-frequency excitation pulse, followed by a gradient **G** (measured as frequency per unit distance) acting for a short time τ that phase-encodes the initial position $\mathbf{r}_0$ of each spin. A second gradient is applied after a time Δ which refocuses the effects of the initial gradient pulse, provided the spins have not moved. If they have, refocusing is generally incomplete, and the resulting phase dispersion will cause a motion-dependent echo attenuation which depends on the displacement $\Delta\mathbf{r}$. The echo peak intensity is usually expressed either in terms of the conditional probability $P(\mathbf{r}_0|\mathbf{r}_0 + \Delta\mathbf{r}, \Delta)$ of migration weighted by the sample density $\rho(\mathbf{r}_0)$ (*12, 13*) or, equivalently, as the joint probability $P_\Delta(\mathbf{r}_0, \Delta\mathbf{r})$ that a particle initially at $\mathbf{r}_0$ undergoes a displacement $\Delta\mathbf{r}$ during the time Δ. Neglecting motion during the gradient pulses, the spin-echo peak is given by

$$S_\Delta(\mathbf{q}) = \int\int P_\Delta(\mathbf{r}_0, \Delta\mathbf{r})\exp(2\pi i\mathbf{q}\cdot\Delta\mathbf{r})d\mathbf{r}_0 d\Delta\mathbf{r}, \quad [1]$$

where $\mathbf{q} = \mathbf{G}\tau$ is the strength of the gradient pulses in cycles per unit distance. Equation [1] demonstrates an intimate relationship between the intensity of the echo $S_\Delta(\mathbf{q})$ and the reduced displacement probability $\bar{P}_\Delta(\Delta\mathbf{r}) = \int P_\Delta(\mathbf{r}_0, \Delta\mathbf{r})d\mathbf{r}_0$, in that the peak signal $S_\Delta(\mathbf{q})$ directly samples $\langle\exp(2\pi i\mathbf{q}\cdot\Delta\mathbf{r})\rangle$, the statistical characteristic function of the variable $\Delta\mathbf{r}$ (*14*). Hence, as initially shown by Kärger and Heink (*15*), $\bar{P}_\Delta(\Delta\mathbf{r})$ is available by Fourier transformation of echo peaks with respect to gradient pulse strength. The usefulness of this stepped-gradient procedure for characterizing motion has since been established in a number of studies (*16–20*).

This specific approach differs from velocity imaging techniques (*21–24*) in two significant respects. First, rather than characterizing motion in terms of a single velocity value, the complete displacement distribution is presented. Second, and more importantly, this procedure describes total particle displacement instead of pointwise velocity. In the parlance of fluid mechanics, pulsed-gradient NMR techniques provide a Lagrangian, rather than Eulerian, experimental description of flow (*25*). This fact makes NMR extremely well suited for studying global flow properties, unlike alternative techniques such as laser Doppler anemometry, which provide local flow information and can only trace long-term flow behavior after painstaking pointwise sampling and numeric integration.

* Department of Chemistry, University of Georgia, Athens, Georgia 30602.

† Department of Physics, Massachusetts Institute of Technology, Cambridge, Massachusetts 02139.

‡ To whom correspondence should be addressed.

1064-1858/93 $5.00

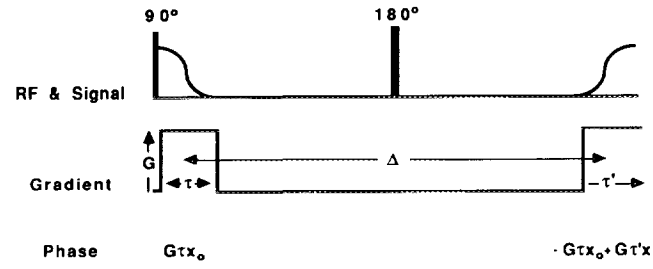

FIG. 1. Basic pulse-gradient spin-echo sequence, showing the phases imposed on the spins during the different stages of the experiment for initial and final particle locations x_0 and x_1.

Relatively few works (*26*) have attempted to extract flow information from distortion of echo shapes caused by motion in a gradient. We show in the present work how a stepped-pulsed-gradient analysis applied to the entire echo can retrieve the complete, spatially resolved, Lagrangian displacement distribution $P_\Delta(\mathbf{r}_0, \Delta\mathbf{r})$. In the following section, we discuss how the correlation or joint distribution between molecular positions and displacements is encoded in echo shapes and discuss an NMR experiment for its extraction. The instrumental and data-processing procedures that were used to implement this experiment are then described and the following section shows results that are obtained for the case of Taylor–Couette flow. Finally, we discuss general features of the present experiment compared with other flow-measuring techniques and suggest some possible extensions.

POSITION–DISPLACEMENT CORRELATIONS

We begin with analysis of phase development in the PGSE experiment shown in Fig. 1. After an initial 90° radiofrequency pulse, a gradient pulse G is applied along the x direction for a time τ, and a spin located in the $x = x_0$ plane acquires a phase ϕ_0 given by

$$\phi_0(G) = G\tau x_0. \qquad [2]$$

(To avoid carrying redundant factors of 2π, we measure angles in units of cycles and gradients in units of frequency per unit length.) When after a time delay Δ a second identical gradient pulse is applied, the spin develops an additional phase at a rate that depends on its new location x_1. Since the intermediate 180° RF pulse reverses the phase acquired during the first pulsed gradient, the total phase at a time τ' into the second pulse will be given by

$$\phi_\Delta(G, \tau') = -G\tau x_0 + G\tau' x_1. \qquad [3]$$

This phase can be rewritten as

$$\phi_\Delta(k, q) = kx_0 + q\Delta x, \qquad [4]$$

where

$$k = G(\tau' - \tau)$$
$$q = G\tau' \qquad [5]$$

are identified as wavenumbers which encode the initial position x_0 and the particle displacement $\Delta x = x_1 - x_0$. In the PGSE experiment, attention is confined to the intensity of the signal at the top of the echo where $\tau = \tau'$. At that instant, k vanishes, and as is well known, the signal purely reflects particle displacements. However, if the entire echo formation and decay during the second gradient pulse are digitized, then the data points $S_\Delta(G, \tau')$ phase-encode $P_\Delta(x_0, \Delta x)$ (the joint probability that a particle initially at x_0 undergoes a displacement Δx) according to the relation

$$S_\Delta(G, \tau') = \iint P_\Delta(x_0, \Delta x)\exp[2\pi ik(G, \tau')x_0] \times \exp[2\pi iq(G, \tau')\Delta x]dx_0 d\Delta x. \qquad [6]$$

In this form, we see that S_Δ is a discrete sampling of the two-dimensional characteristic function $\chi(k, q)$ (*14, 20*) of the random variables $(x_0, \Delta x)$, defined as

$$\chi(k, q) = \langle \exp[2\pi i(kx_0 + q\Delta x)] \rangle. \qquad [7]$$

Consequently, $P_\Delta(x_0, \Delta x)$ can be reconstructed by careful Fourier analysis of gradient-echo-shape data. Equation [6] shows that $S_\Delta(G, \tau') = \chi[G(\tau' - \tau), G\tau']$ and predicts exactly how an echo generated in (G, τ') space samples (k, q) space. There are two characteristic features. The first is that because the echo shape is formed with τ' increasing and with the gradient level G fixed, each echo acquisition samples a diagonal path in (k, q) space as shown in Fig. 2 (top). Second, echoes acquired with identical dwell times (i.e., uniformly spaced values of τ') but different gradient levels have spacings in (k, q) space proportional to the increments of the gradient G used in forming the echo.

This situation differs from conventional 2D NMR, where data are automatically acquired on an orthogonal grid composed of equally spaced points, for which processing by a fast Fourier transform (FFT) (*27*) is straightforward. Nevertheless, it is still possible to ensure that a rectangular grid is generated here as well. Equation [5] shows that diagonals of such a lattice can be generated by a set of acquisitions for which both gradient pulse levels G are stepped in uniform increments each time by ΔG and for which the echo sampling dwell times $\Delta\tau'$ are adjusted for each gradient level according to

$$\Delta\tau'_n(G) = n\tau\Delta G/G, \qquad [8]$$

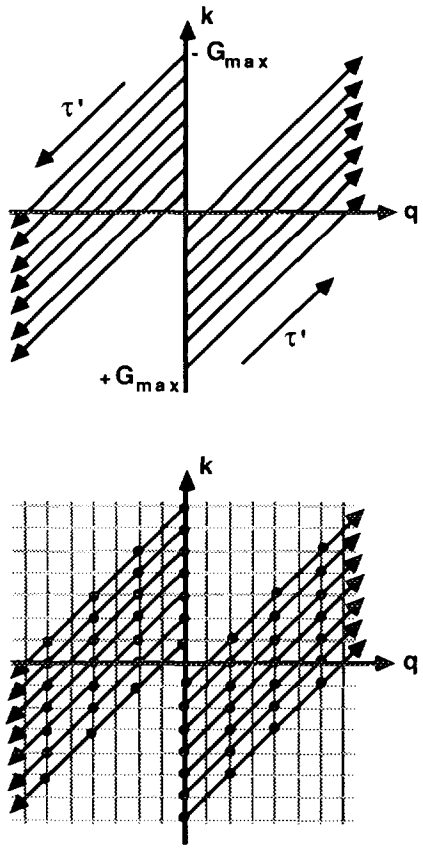

FIG. 2. (Top) Trajectory of the system in (k, q) space during a PGSE experiment, as a function of the experimental parameters $-G_{max} \leq G \leq G_{max}$ and τ' for a series of stepped-gradient values. (Bottom) Distribution of data points on a (k, q) space lattice obtained by coordinating the dwell time in τ' with the values of G, illustrated for the case $n = 2$ (see Eq. [7]). A 2D FFT can be applied directly to the data once they have been rearranged into this regular grid.

where n is an arbitrary fixed integer. Figure 2 (bottom) illustrates the digitized points for the case where $n = 2$. In general, this procedure generates a grid with unit cell

$$(\delta k, \delta q) = \Delta G \tau (n, 1). \qquad [9]$$

Just as in ordinary spectroscopy, the density and range over which the signal must be sampled are related to the extent of the "spectrum" $P_\Delta(x_0, \Delta x)$. Resolution in (k, q) depends on the specimen size, range(x_0), and on the range of displacements, range (Δx), according to

$$\delta k = \frac{1}{\text{range}(x_0)}; \qquad \delta q = \frac{1}{\text{range}(\Delta x)}. \qquad [10]$$

Given Eqs. [5] and [10], the total ranges covered in the x_0 and in the Δx dimensions are

$$\text{range}(x_0) = \frac{1}{\Delta G \tau}, \qquad \text{range}(\Delta x) = \frac{1}{n \Delta G \tau}. \qquad [11]$$

Although Eq. [8] fails to define the sampling time for the $G = 0$ experiment, any single point (at any τ') can be acquired for this null gradient because, in principle, the signal for this case does not evolve. In practice, with reasonably homogeneous magnetic fields, it lasts sufficiently long that amplitude of the single point sampled in the $G = 0$ case varies negligibly with the instant of sampling.

The domain over which S_Δ extends is determined by the fineness of features δx_0 along the spatial dimension and by the smallest displacement structure $\delta(\Delta x)$ along the motion dimension. Displacement structure is generally the finer of the two, and this requires that the gradient be stepped up to a maximum value G_{max} given by

$$q_{max} = \text{range}(q) \cong G_{max} \tau \cong \frac{1}{\delta(\Delta x)}. \qquad [12]$$

In the preceding discussion we have shown how slice-resolved motion statistics are encoded in pulsed-gradient echo shapes and how they may be obtained by a conventional FFT of appropriately sampled and rearranged data. We now discuss a specific experimental example of $P_\Delta(x_0, \Delta x)$ position–displacement distributions obtained with this method.

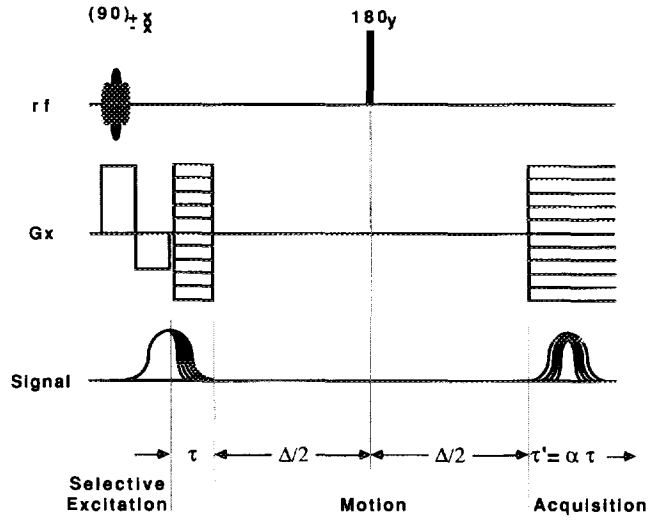

FIG. 3. Pulse sequence employed to obtain the position–displacement correlation spectra. The experiment is performed on a slab of fluid excited each time by an amplitude-modulated prepulse. A series of echoes, each corresponding to one of a series of gradient pulse levels, are digitized and then processed as described in the text.

A PROCESSING EXAMPLE

The experiments discussed throughout were carried out on a Nalorac 4400 Imaging Spectrometer based on a 4.2 T superconducting magnet and controlled by a microVAX GPX Workstation. Images of both static and flowing water were obtained using the sequence shown in Fig. 3. The sequence starts with an on-resonance 90° eight-lobe sinc pulse applied in the presence of a gradient to excite the spins in a 14 mm slab near the center of the coil, followed immediately by a reversed-gradient phase-refocusing pulse. The initial positions of the nuclei are then encoded by a 1 ms gradient pulse applied in the direction along which motion is to be monitored. A 180° pulse, compensated for RF inhomogeneity (*28*), is applied after a time delay $\Delta/2$ to invert the phase of the spins. After a second delay $\Delta/2$, the refocusing gradient is applied, at which time acquisition of the shape of the reforming echo is begun at the gradient-dependent sampling rate prescribed by Eq. [8]. Here, the index n was set to 3, so the spatial range along the x_0 axis was three times larger than that along Δx. Phase alternation of the initial 90° pulse and receiver was used to suppress artifacts. The final $S(G, \tau')$ data set before arrangement consisted of 128 64-point FIDs, acquired using 128 gradient levels whose values (calibrated to within 10% with a phantom) ranged between ±30 kHz/cm.

Each acquisition began at the start of the second gradient pulse. The termination point of the sampling is unimportant as long as the entire echo is sampled. We set the acquisition length here by sampling the same number of points for all scans; acquisitions therefore terminated at a q = constant locus indicated by the heads of the arrows in Fig. 2 in the (k, q) domain. Special care was necessary to ensure that all echo peaks formed by the refocusing gradients fell within ±1 μs of their nominal 1 ms refocusing time, since the large-gradient echoes were very narrow and even slight peak misalignments produced noticeable distortion. Shifts in echo peaks caused by eddy currents and similar rise-time delays were compensated by programming small run-time changes in the durations of the initial space-encoding pulsed gradients.

Once the data set $S(G, \tau')$ was acquired, it was rearranged into (k, q) space as described above and 2D Fourier transformed. A magnitude calculation was finally applied to remove first-order phase distortions associated with the echo delays.

As an example, Fig. 4 illustrates the three stages of data processing required to obtain a two-dimensional x_0–Δx NMR correlation spectrum for a static sample. The topmost plot shows the magnitude of the data as acquired, consisting of a series of echoes formed by gradient pulses with increasing strengths. Two features are apparent; first, the echo peaks migrate away from the $t = 0$ point as the gradient magnitudes increase, and second, the echo widths are approximately

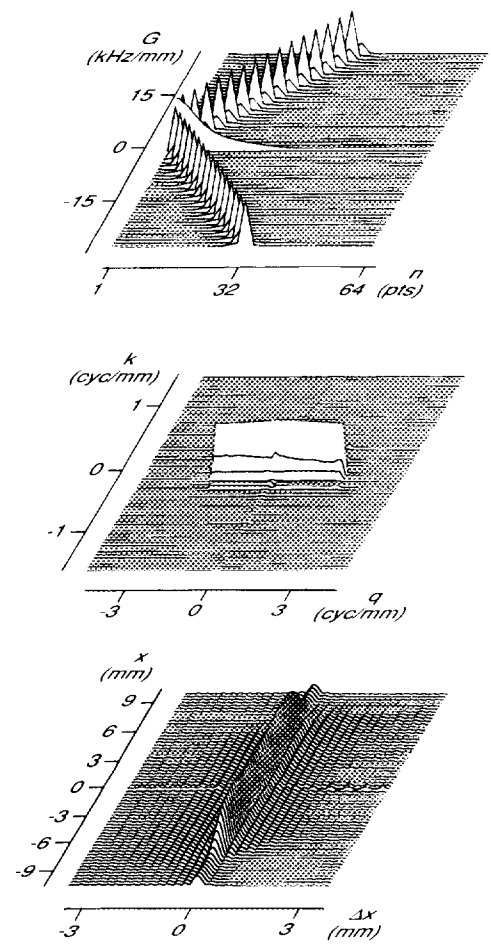

FIG. 4. Magnitude displays of the different stages taking place as the signal $S(G, \tau')$ is processed to yield a 2D x–Δx correlation spectrum. (Top) Plot of the 2D series of echoes as acquired by the spectrometer on a sample of static water, as a function of gradient level G and of its sampling point in the signal digitizer. Although all echoes form at $\tau' = 1.00$ ms, the buffer location where the peaks occur migrates since sampling times are varied with gradient level. Due to the $n = 3$ factor used in Eq. [8] to determine the dwell times, echo centers were digitized only every other gradient scan (see Fig. 2). (Center) The same data set after rearrangement onto the (k, q) domain. The data are severely truncated along the q direction for this motionless sample. (Bottom) The $P_\Delta(x_0, \Delta x)$ displacement distribution obtained by FFT of the (k, q)-domain data, showing the narrow ridge at $\Delta x = 0$ along the sample length.

constant. Both effects arise from setting dwell times for each scan in inverse proportion to each scan's gradient level, as prescribed by Eq. [8]. Since in all cases the duration of the first gradient pulse is fixed, the physical time between the start of acquisition and the echo peak is constant. Thus the number of points acquired between these two events will increase as gradient levels rise and dwell times are reduced. Likewise, because the echo lifetime is inversely proportional to the gradient strength, the actual narrowing of the echo with increasing gradient strength is exactly compensated by the increased sampling rate.

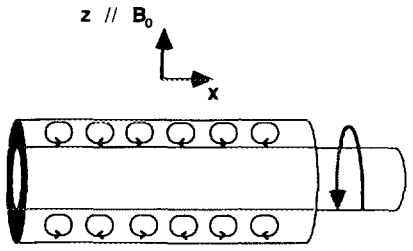

FIG. 5. Coordinates and geometry employed to create the Taylor vortices. The outer cylinder (not shown) has a 12.7 mm inner diameter, the inner cylinder is a rotating rod 6.3 mm in diameter, and the total sample length is about 50 mm. The circulation patterns represent the square-like Taylor vortex cells which are superimposed on azimuthal Couette flow circulating around the common cylinder axis. An NMR transmit/receive coil, approximately 40 mm long, is wound about the outer cylinder.

Figure 4 (center) shows echo data after mapping from (G, τ) space to (k, q) space according to Eq. [5]. The data which represent the characteristic function of the displacement distribution are a sharp ridge lying along the q axis in the Fourier domain, indicating a large sample extent and sharp displacement distribution.

The experimental displacement image obtained by calculating the magnitude of the FFT of this (k, q)-domain signal is shown in Fig. 4 (bottom). The joint distribution $P_\Delta(x_0, \Delta x)$ is a sharp ridge extending from -7 to $+7$ mm along the x axis. It consists of a ridge parallel to the x axis, whose height is proportional to the density of the particles in the sample and whose width is given by the extent of the displacements. This shape is as expected and shows that initial particle positions x_0 are evenly distributed within the slice-selected 14 mm long plug near the detector coil center, whereas Δx is distributed sharply about 0. Artifacts in the form of small ridges appear parallel to the main $\Delta x = 0$ ridge because of severe data truncation along the q dimension evident in the k–q plot. Unlike more familiar star artifacts in 2D NMR to which these are related, these extend diagonally rather than laterally from the central ridge.

TAYLOR VORTEX RESULTS

This technique was applied to a water sample undergoing Taylor–Couette flow to examine characteristics of the distribution $P_\Delta(x_0, \Delta x)$ in a flowing system. The Taylor vortices were generated in a homebuilt probe by placing a water sample between rotating inner and stationary outer cylinders as indicated in Fig. 5 (*29–31*). The cylinder diameters were 6.3 and 12.5 mm, respectively. The apparatus axis was oriented horizontally in the vertical superconducting magnet bore, and the length of the fluid cylinder confined between O-ring seals at the ends was approximately 5 cm. A toothed gear attached to the protruding end of the inner rod was connected by a belt drive to a commercial motor-controller system with a speed accuracy better than 1% (*32*). Taylor vortices appeared at a critical rotation frequency of 1.1 Hz. Higher instabilities were neither observed nor predicted up to the maximum 5 Hz rotation rate used in this study. Gradient coils, directly potted onto mounting blocks holding the cylinder/rod arrangement, provided field gradients along the axial x direction, i.e., along the fluid symmetry axis perpendicular to B_0. The experiment therefore correlates axial positions and axial displacements; motion of the azimuthal Couette flow was unobservable.

Figures 6, 7, and 8 show the data for Taylor–Couette flow, for various delays Δ between pulsed gradients and for 4, 2, and 5 Hz inner-cylinder rotation rates, respectively. The x axes of the figures indicate starting locations along the common axis of the confining cylinders, and the Δx axes indicate displacements along this same axial direction. Each of the 128 stacked plots in the slab-selected region from -7 to $+7$ mm shows the particle displacement distribution for a corresponding slice, whose initial location x_0 may be read off the axes to the left. The behavior of these displacement im-

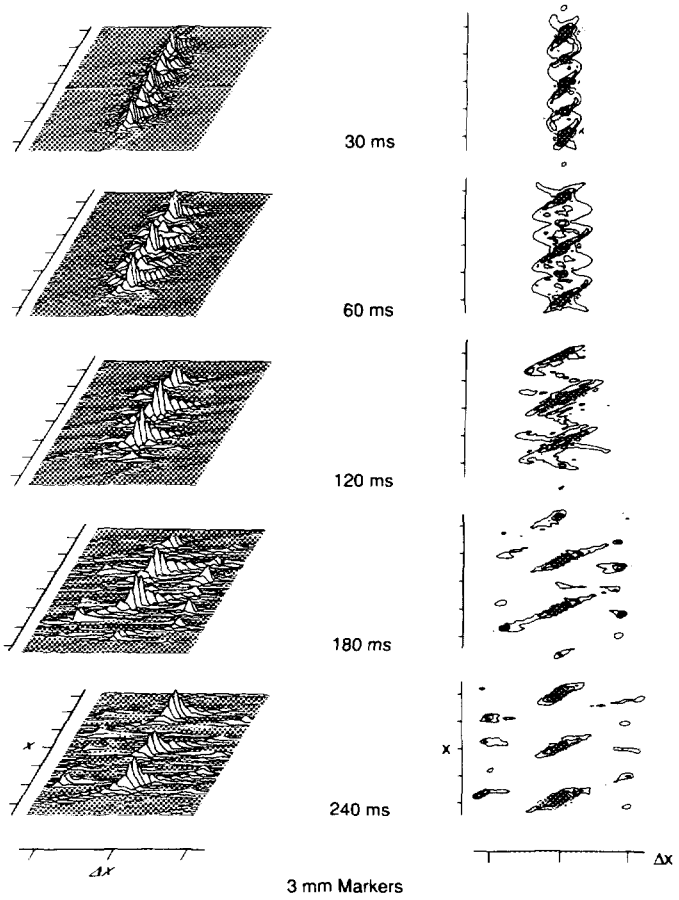

FIG. 6. Stacked (left) and contour (right) images of the Taylor vortex displacements as a function of the indicated delays between the initial and the refocusing gradient pulses. Spectra were recorded using the pulse sequence shown in Fig. 3 while spinning the inner rod of the assembly at 4 Hz, corresponding to a Taylor number T = 80,000. All markers are 3 mm apart.

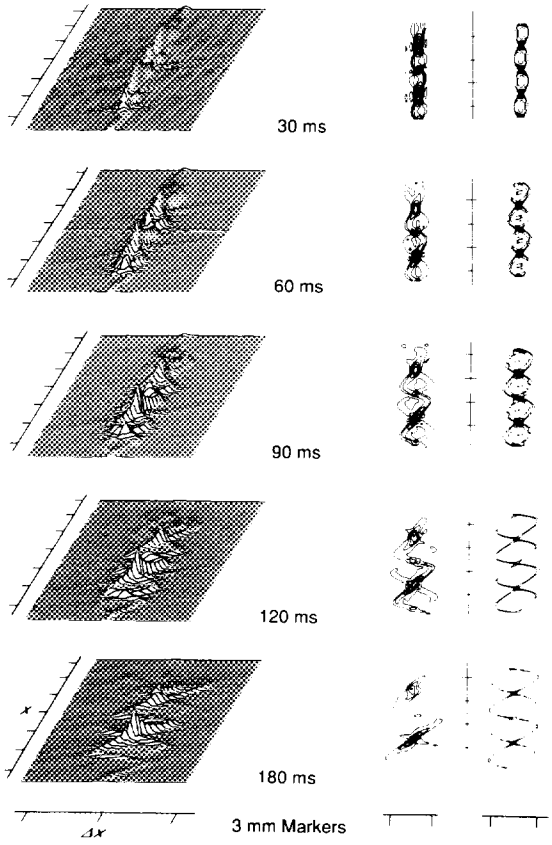

FIG. 7. Experimental (left and center) and simulated (right) images of Taylor vortex displacements as a function of the delay between the initial and the refocusing gradient pulses. The inner rod was spun at 2 Hz (Taylor number T = 20,000). Simulations were obtained as described in the Appendix using the indicated times and $a = b = 10$, which corresponds to a maximum speed v_{max} = 69 mm/s achieved at a radial position r_{max} = 4.7 mm. All markers are 3 mm apart.

ages is consistent with the flow pattern shown in Fig. 5. We would expect plots taken for short times, for which little motion has occurred, to show a single ridge similar to that in Fig. 4 (bottom). This localized structure also persists for slices initially near adjacent cell boundaries or "edges," since their motion is perpendicular to the gradients; this accounts for the succession of peaks at the intersection of the ridges and allows the position of cell edges to be located on the initial-position x scale to the left of the plots. On the other hand, displacements for slices initially within cell interiors evolve rapidly because axial motions are present from the outset. Because velocities in such an interior slice are simultaneously parallel and antiparallel to the gradient direction depending on radial particle location, the initial diffusion ridge splits to reflect the bimodal velocity distribution. The motion generates a series of chain-shaped ridges, whose links meet at locations corresponding to cell boundaries.

Asymmetric details which reflect the distinctively Lagrangian character of the NMR displacement statistics are superimposed on this basic structure. These include alternating intensities of the cell-edge peaks, differences between the intensities of the ridges that correspond to opposing displacements within the vortex cells, the asymmetric twisting of these displacement ridges with respect to the center of the cells, and the small peaks appearing at later times at displacements corresponding to approximately one cell length, appearing in the advanced development shown in Fig. 6.

These displacement asymmetries at first appear to be inconsistent with obvious velocity symmetries, but agreement between experimental distributions shown in the leftmost columns of Figs. 7 and 8 and simulations shown in the rightmost columns (derived in the Appendix) is actually very good. The only discrepancies are weak diagonal ridges emanating from the main peaks whose origin was explained at the end of the previous section.

These asymmetries are consequences of the Lagrangian character of the displacement distributions. From the Eulerian point of view, which considers the velocity field, we observe that the x velocity component is antisymmetric when

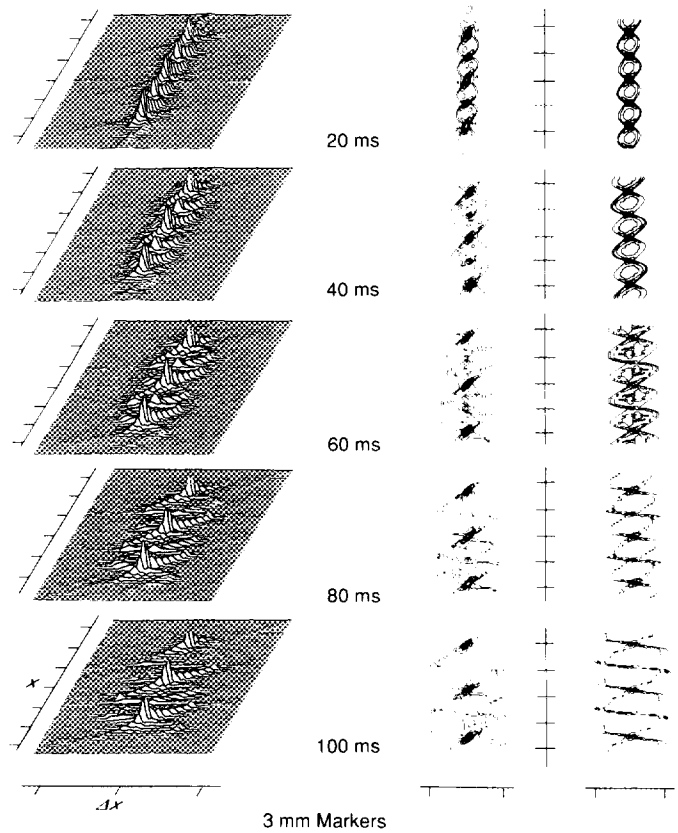

FIG. 8. Experimental (left and center) and simulated (right) images of Taylor vortex displacements as a function of the delay between the initial and the refocusing gradient pulses. The inner rod was spun at 5 Hz, which for the present geometry corresponds to a Taylor number T = 125,000. Simulations were obtained using $a = 50$, $b = 30$, corresponding to v_{max} = 226 mm/s, r_{max} = 4.8 mm. All markers are 3 mm apart.

reflected about cell edges but symmetric when reflected about centers. This velocity symmetry is in fact apparent in the very-short-time displacement data, where displacements and velocities are approximately in proportion according to $\Delta x = v_x\Delta$. Because significant acceleration accompanies vortex motion, however, this first-order approximation soon fails, and Lagrangian considerations of displacements lead to a somewhat different picture. To reconcile these two viewpoints, one must consider the exact expression

$$\Delta x(T) = \int_0^T dt v_x[\mathbf{r}(t)]. \qquad [13]$$

As the particle migrates from its initial position, its time development is determined by the pointwise velocity field along its trajectory, rather than simply the velocity at its initial location. This relationship between velocity and displacement highlights the central difference between Lagrangian and Eulerian descriptions and predicts that only antisymmetric velocity symmetry will generate any related symmetry in Δx.

Figure 9 shows a schematic (x, v_x) "phase-space" diagram for motion representative of particles located at planes of velocity symmetry and antisymmetry. For the symmetric case in Fig. 9A, describing motion of fluid initially near a cell wall, particles decelerate as they approach the cell edge, shown as the origin, and accelerate afterward. The progress of particles toward the origin is therefore markedly slower than that for departure, so displacements on opposite sides of the origin will develop at different rates. This is why successive edge peaks in Figs. 7 and 8 have alternating amplitudes: x deceleration occurs for fluid at outgoing cell edges approaching the stationary outer cylinder wall, but x acceleration occurs for fluid moving radially inward.

On the other hand, the antisymmetric velocity field depicted in Fig. 9B, corresponding to fluid initially at a Taylor cell center, is different. Here, particles on opposite sides of the origin do move in equivalent velocity fields, albeit in opposite directions. Hence, we expect antisymmetric velocity symmetries to assert themselves as antisymmetric displacement distributions.

Based on these arguments, the only symmetry expected is inversion symmetry of the displacement distribution about each peak at a cell edge. The data are entirely consistent with this expectation, even for the rather long flow stages shown in Fig. 6. Note that the ingoing cell edge peaks disappear, but that the larger peaks of the outgoing edges persist. The appearance in the experimental data of small peaks located at displacements of about one cell length also appear for longer delays; this is because an appreciable population of molecules initially located at one cell edge flows to and remains at an adjacent edge.

These results exemplify how Lagrangian displacement descriptions can be more informative than simpler Eulerian

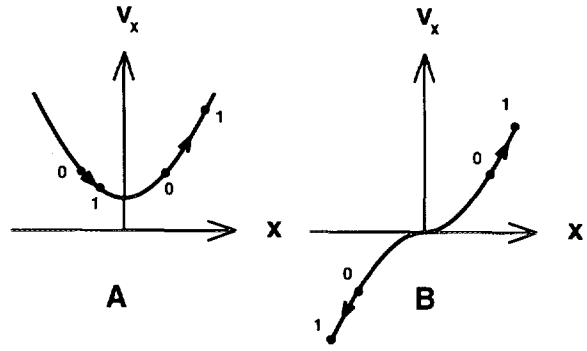

FIG. 9. Displacement behavior for symmetric (A) and antisymmetric (B) velocity distributions. In (A), particles initially related by reflection symmetry sample different velocity fields and their displacement fail to reflect the symmetry of the velocity field. In (B), on the other hand, particles related by antisymmetry have similar velocity histories, so their displacements develop the same reflection symmetry as the velocities.

velocity characterizations: the displacement distributions show rich time development even though the velocity is time independent. In particular, one can determine how long it takes for fluid at one cell edge to migrate to another, simply by observing when the satellite peaks appear as in Fig. 6. While this information is available in principle from velocity measurements, timing displacements in this way requires measurement of a sufficiently large number of pointwise values of v_x to approximate the integral Eq. [13], to obtain Δx as a function of T, followed by numerical inversion of this relation to find T as a function of Δx.

DISCUSSION AND CONCLUSIONS

In the preceding sections we have introduced and exemplified a 2D NMR technique that correlates initial particle positions in a fluid with displacements at later times. While the acquisition and processing of the data are unconventional, simulations showed that the results obtained with this method describe complex flows quite accurately. Compared with NMR techniques proposed earlier for the characterization of flow, in which two-dimensional experiments were required to obtain the displacements of a single x_0 slice (*16–18*), the information available from the experiment described above represents a reduction in acquisition time from 3D to 2D NMR, which conservatively is about an order of magnitude.

There are at least two other possible improvements to the NMR experiment described here. On one hand, it is possible to combine it with recently developed (*20*) multiple-pulsed-gradient spin-echo methods to obtain complete histories of the displacements within a fluid (as shown in Figs. 6–8) from a *single* 2D NMR experiment. In addition, the relatively high signal-to-noise ratios that characterize the statistical images obtained for $P_\Delta(x_0, \Delta x)$ suggest that it is still possible to introduce a third dimension to the pulse sequence and at

the same time keep the total duration of the experiment within reasonable limits. In this respect, work is under way to explore the addition of a molecular order parameter into the experiment described in the present study.

We have shown how echo-shape analysis in particular and PGSE NMR in general differ from laser Doppler anemometry, not simply because they are applicable to opaque systems, but more significantly because NMR focuses on displacements of fluid elements rather than on velocities at points in the flow field. Global flow properties such as the time required for particles to rearrange themselves, and even the occurrence of circulation, are easily observable from this Lagrangian measurement. The statistical character of this experiment not only allows one to obtain displacement distributions in the sample from a single (30 minute) experiment but also provides a particularly well-suited technique for characterizing complex flow in systems such as biological or polymeric fluids.

APPENDIX

The starting point for evaluating the probability that after a time Δ particles initially at $\mathbf{r}_0$ will have moved a distance $\Delta\mathbf{r}$ are the Navier–Stokes equations for an incompressible Newtonian fluid. For simplicity, we neglect the effects of viscosity and write these equations (*33*) in the cylindrical coordinates shown in Fig. 5,

$$\frac{\partial u}{\partial t} + (\mathbf{u}\cdot\nabla)u_r - \frac{u_\theta^2}{r} = -\frac{\partial}{\partial r}\left(\frac{p}{\rho}\right),$$

$$\frac{\partial u_\theta}{\partial t} + (\mathbf{u}\cdot\nabla)u_\theta + \frac{u_\theta u_r}{r} = -\frac{1}{r}\frac{\partial}{\partial\theta}\left(\frac{p}{\rho}\right),$$

$$\frac{\partial u_x}{\partial t} + (\mathbf{u}\cdot\nabla)u_x = -\frac{\partial}{\partial x}\left(\frac{p}{\rho}\right), \qquad [A1]$$

where p, ρ, and $\mathbf{u}$ are, respectively, the pressure, density, and velocity of the fluid. When the liquid is contained between two concentric cylinders r_1 and r_2 and the inner cylinder is rotating with an angular velocity Ω_1, these equations admit a stationary solution of the form

$$u_r = u_x = 0,$$

$$u_\theta(r) = Ar + B/r, \qquad [A2]$$

where $A = -\Omega_1 r_1^2/(r_2^2 - r_1^2)$ and $B = \Omega_1 r_1^2 r_2^2/(r_2^2 - r_1^2)$.

The Couette flow predicted by Eq. [A2] persists as long as the angular momentum per unit mass increases monotonically along the radial direction. At high Ω_1 rates, however, this radial momentum gradient reverses sign and instabilities in the motion of the fluid appear, in the form of the Taylor vortices shown in Fig. 5. Although for the purpose of evaluating the $P_\Delta(x_0, \Delta x)$ distributions it is possible to disregard the effects of radial and azimuthal motions within the plane of the applied x field gradients, it is still necessary to find expressions for both the radial and the longitudinal components of the velocities.

For our simulations we used the same flow field as that discussed by Chandrasekhar in his linear analysis of the Taylor instability (*33*). He examines modes which are sinusoidal along the rotation axis, having the form

$$u_x(x, r) = v(r)\cos(kx)$$

$$u_r(x, r) = w(r)\sin(kx), \qquad [A3]$$

where $v(r)$ and $w(r)$ are the radial velocity dependencies related by one of the Navier–Stokes equations,

$$\frac{d}{dr}v(r) + \frac{v(r)}{r} = -kw(r). \qquad [A4]$$

and k is a wavenumber defined by the length of the cells along the x axis. With the aid of the boundary conditions of the radial velocity at the walls of the inner ($r = r_1$) and outer ($r = r_2$) cylinders,

$$v(r_1) = v(r_2) = 0$$

$$v'(r_1) = v'(r_2) = 0, \qquad [A5]$$

the Navier–Stokes equations can be solved to yield numerical solutions of v as a function of r (*33*). Another feature of these solutions is that $v(r)$ is not symmetric about the $r = (r_1 + r_2)/2$ annulus; i.e.,

$$v''(r_1) \neq v''(r_2). \qquad [A6]$$

Since the ultimate goal of the present study is to investigate the flow distributions qualitatively, we decided to simplify our calculations by approximating $v(r)$ with a simple polynomial compatible with Eqs. [A5] and [A6]:

$$v(r) = (r - r_1)^2(r - r_2)^2(ar + b). \qquad [A7]$$

This function has two adjustable parameters a and b, and over a considerable range of these parameters Eq. [A7] closely resembles previously published functions obtained by numerical solution of the Taylor problem (*33*). With this functional dependence of $v(r)$, Eqs. [A3] and [A4] allow one to obtain the velocities $u_x(x, r)$ and $u_r(x, r)$. These can then be integrated to provide the x coordinate of any molecule in a Taylor cell after a time delay Δ. A program was written to compute the $P_\Delta(x_0, \Delta x)$ distribution predicted by these velocities within a single cell, using a and b as adjustable parameters and with diffusion simulated by a triangular spread function whose half-height at half-width is equal to

the width of the exact Gaussian process. Symmetries of the Taylor vortices along x allowed us to extend these single-cell $x_0-\Delta x$ correlation spectra to a whole sample, yielding the complete simulations shown in Figs. 7 and 8.

ACKNOWLEDGMENTS

We are especially grateful to Professor Alex Pines for his helpful suggestions and encouragement throughout the present study. This work was supported by the Director, Office of Energy Research, Office of Basic Energy Sciences, Materials Sciences Division, of the U.S. Department of Energy, under Contract DE-AC03-76SF00098.

REFERENCES

1. L. W. Reeves, *in* "Dynamic Nuclear Magnetic Resonance" (L. M. Jackman and F. A. Cotton, Eds.), pp. 83–180, Academic Press, New York, 1975.
2. D. W. Jones and T. F. Child, *in* "Advances in Magnetic Resonance" (J. S. Waugh, Ed.), Vol. 8, p. 123, Academic Press, New York, 1976.
3. M. A. Hemminga, *in* "Biomedical Magnetic Resonance" (T. L. James and A. R. Margoulis, Eds.), pp. 157–184, Radiology Research and Education Foundation, 1984.
4. P. T. Callaghan, "Principles of Nuclear Magnetic Resonance Microscopy," Oxford University Press, New York, 1991.
5. H. Y. Carr and E. M. Purcell, *Phys. Rev.* **94,** 630 (1954).
6. G. Deville and A. Landesman, *J. Phys.* **32,** 67 (1971).
7. P. DeGennes, *Phys. Lett. A* **29,** 20 (1969).
8. K. Fukuda, Y. Imai, and A. Hirai, *Biotelem. Patient Monitoring* **5,** 223 (1978).
9. J. H. Walton and M. S. Conradi, *Magn. Reson. Med.* **4,** 274 (1987).
10. E. O. Stejskal and J. E. Tanner, *J. Chem. Phys.* **42,** 288 (1965).
11. P. Stilbs, *Prog. NMR Spectrosc.* **19,** 1 (1987).
12. J. Kärger, H. Pfeiffer, and W. Heink, *in* "Advances in Magnetic Resonance" (J. S. Waugh, Ed.), pp. 1–89, Academic Press, New York, 1988.
13. E. O. Stejskal, *J. Chem. Phys.* **43,** 3597 (1965).
14. E. Parzen, "Modern Probability Theory and Its Applications," Wiley, New York, 1960.
15. J. Kärger and W. Heink, *J. Magn. Reson.* **51,** 1 (1983).
16. P. T. Callaghan, C. D. Eccles, and Y. Xia, *J. Phys. E* **21,** 820 (1988).
17. P. T. Callaghan, D. MacGowan, K. J. Packer, and F. O. Zelaya, *J. Magn. Reson.* **90,** 177 (1990).
18. P. T. Callaghan and Y. Xia, *J. Magn. Reson.* **91,** 326 (1991).
19. D. G. Cory and A. N. Garroway, *Magn. Reson. Med.* **14,** 435 (1990).
20. L. Frydman, G. A. Barrall, J. S. Harwood, and G. C. Chingas, *in* "NMR Microscopy: History, Theory and Applications" (B. Blümich and W. Kuhn, Eds.), pp. 938–940, VCH, Weinheim, 1992.
21. A. Caprihan and E. Fukushima, *Phys. Rep.* **198,** 193 (1990).
22. P. R. Moran, *Magn. Reson. Imaging* **1,** 197 (1982).
23. A. N. Garroway, "Proceedings, XVIIIth Ampere Congress," Nottingham, p. 435, 1976.
24. J. R. Singer, *Science* **130,** 1652 (1959).
25. H. Lamb, "Hydrodynamics," Dover, New York, 1945.
26. R. J. Hayward, K. J. Packer, and D. J. Tomlinson, *Mol. Phys.* **23,** 1083 (1972).
27. R. R. Ernst, G. Bodenhausen, and A. Wokaun, "Principles of Nuclear Magnetic Resonance in One and Two Dimensions," Oxford Univ. Press, London, 1990.
28. R. Tycko, H. M. Cho, E. Schneider, and A. Pines, *J. Magn. Reson.* **61,** 90 (1985).
29. R. C. DiPrima and H. L. Swinney, *in* "Hydrodynamic Instabilities and the Transition to Turbulence" (H. L. Swinney and J. P. Golub, Eds.), pp. 139–180, Springer-Verlag, New York, 1981.
30. G. I. Taylor, *Phil. Trans. R. Soc. London A* **1923,** 289 (1923).
31. M. Vera and J. B. Grutzner, *J. Am. Chem. Soc.* **108,** 1304 (1986).
32. ElectroCraft Corp., 1600 Second Street South, Hopkins, Minnesota 55343.
33. S. Chandrasekhar, "Hydrodynamic and Hydromagnetic Stability," Dover, New York, 1981.